

Quantitative measurements of daytime near infrared sky brightness at the AEOS 3.6 m telescope

Michael Hart, Stuart Jefferies Douglas Hope, James Nagy, Olivier Durney, Robert Codona
HartSCI LLC, 6135 N. Tucson Mountain Dr., Tucson, AZ 85743

Stacie Williams
AFRL/RD, 550 Lipoa Parkway, Kihei, HI 96753

ABSTRACT

We report daytime sky brightness measurements recorded in the near infrared from the 3.6 m AEOS telescope. Measurements were made at various positions in the sky and separation angles from the sun. The detector was an InGaAs focal plane array in a FLIR SC6000 camera, with images taken through a 50 nm wide filter centered at 1250 nm as well as without any optical filter. The brightness measurements have been calibrated by reference to observations of a photometric standard star in the same bands. We discuss how these new results are motivated by the selection of optimal techniques for high-resolution imaging of satellites from the AEOS telescope.

1 MOTIVATION

At first glance it would appear that imaging in the near infrared wavebands between 1 and 2.5 μm has little to contribute to Space Situational Awareness (SSA). Compared to the visible bands, available detectors are noisier, much more expensive, and must be operated at substantially colder temperatures frequently requiring cryogenic equipment. Moreover, the images obtained typically do not add substantially to one's knowledge of space object phenomenology, and, above all, the resolution available through a telescope of a given diameter is poorer. Nevertheless, near IR light carries independent information that may be exploited to enhance the capabilities of systems already operating in shorter bands, while at the same time improving the overall signal-to-noise ratio (SNR).

We are taking this approach in support of a system to carry out high-resolution imaging of space objects during the day at the 3.6 m AEOS telescope on Mt. Haleakala. An imaging sensor in the EO bands, under construction by Boeing LTS, will exploit the aperture partitioning technique of Calef [1]. In parallel, a Shack-Hartmann wave-front sensor (WFS) built by HartSCI will collect simultaneous wave-front information in order to characterize the point-spread function (PSF) independently. The WFS, with selectable subaperture geometry, employs an InGaAs focal plane array (FPA) sensitive from 0.9–1.6 μm and will rely on the near IR light that cannot be used by the imager.

The data from both sensors together will be analyzed by HartSCI's Daylight Object Restoration Algorithm (DORA) [2, 3], designed to deliver high resolution imaging of space objects from large ground-based telescopes under daylight conditions. DORA is in the general class of multi-frame blind deconvolution algorithms that restore high fidelity images from severely blurred data, but it extends the concept to otherwise unreachable levels of atmospheric turbulence strength by relying on the simultaneous WFS data to provide initial estimates of the aberrated PSFs. These form powerful constraints on the image restoration process. DORA has been demonstrated to date with data recorded by the sensors in the AO system at the AEOS telescope, but with the AO system itself not running; an example is shown in Figure 1. In that system, both the imager and the WFS are CCDs, and must share the EO part of the spectrum. However, the low dispersion of the atmosphere in the EO/IR bands allows wave-front measurements made in the IR to be applied to visible light images. (We note too that because the WFS used by DORA is *not* trying to drive a closed-loop AO system, even first-order chromatic differences are easy to take into account with a simple scale factor applied to the computed wave-front slopes.) By operating the WFS in the IR, all the visible light remains available to the imaging channel, and we suffer no SNR penalty in the image data.

Since the new system is expected to operate in full daylight, the sensors must all cope with a bright background illumination. At visible wavelengths, the brightness is already well characterized [4, 5], but there is little available literature on the daytime sky brightness in the near IR, and none of which we are aware that directly addresses the site on Mt. Haleakala that is of present interest. We have therefore made new measurements to quantify the near IR sky brightness from the AEOS telescope. The goal was not to undertake a survey that is in any sense complete across all time scales and viewing geometries, but rather to assure ourselves of the viability of the IR WFS for use

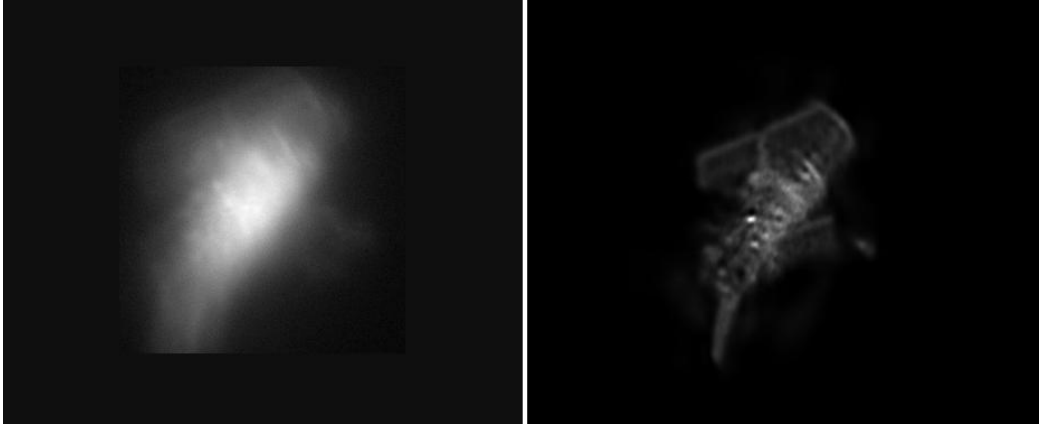


Figure 1. The Hubble Space Telescope. Left: Raw data frame with AO in open loop (integration time of 20 ms, spectral bandwidth of 25% at 0.85 μm). Right: DORA restoration using 20 frames of data.

with DORA. To that end, data were collected during a single day, and we report in this paper the results of the subsequent analysis.

2 METHODOLOGY AND ANALYSIS

2.1 Data collection

Data for the study were acquired at the AEOS telescope during a 2.5 hour period from approximately 10:30 to 13:00 local time on 2014 March 19. Images of the daytime sky were captured by a FLIR SC6000 camera with an InGaAs FPA. In order to avoid saturation from the bright sky background, short exposure times were used in a window of 256×256 pixels within the 640×512 FPA. Each observation comprised a sequence of typically 4000 images taken at frame rates from 60 Hz to 500 Hz. Some of the sequences were recorded with no optical filter in the beam train; the optical bandpass therefore approximately corresponded to 0.9–1.6 μm where the FPA has high quantum efficiency. Additional sequences were taken through a filter centered at 1250 nm, with 50 nm bandpass; the transmission curve is shown in Figure 2. This is in the middle of the J window of high atmospheric transparency. Although the filter did not correspond to a bona fide astronomical J band, it was at least an order of magnitude cheaper and quicker to procure, and photometric calibrations with reasonable accuracy can be made using near-IR standard stars whose colors are close to zero in that part of the spectrum. The full list of 47 observations is reported in the Appendix. Figure 3 shows how they map onto the celestial sphere.

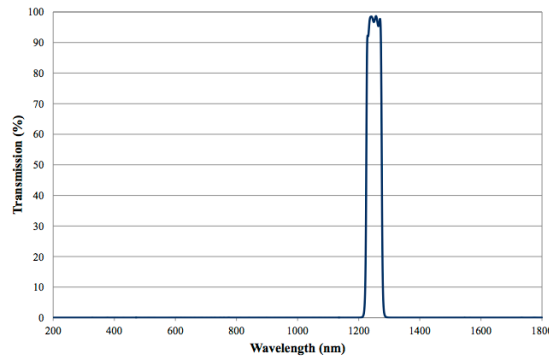


Figure 2. Bandpass for 1250 nm sky brightness measurements [6].

Calibrator stars were drawn from the Bruzual-Persson-Gunn-Stryker (BPGS) catalog of spectroscopic standards [7]. The brightest of these in the data sets, BPGS 97 (HR 7670, a G6 subgiant with, incidentally, two known planets), was used to estimate the background brightness in this study. HR 7670 has near IR magnitudes of $I=4.9$, $J=4.55$, $H=4.24$, $K=4.08$ [8]. The geometry of the star observations is illustrated in Figure 4, which shows the positions of

the sun and the star with respect to the observatory (at the center of the sphere) and the local horizon for two data sets recorded roughly an hour apart.

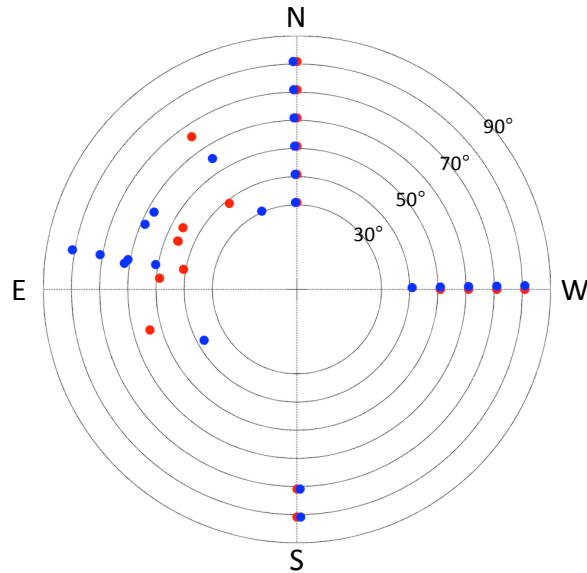


Figure 3. Map of all the observations on sky in azimuth and elevation angle. Blue and red dots show the coordinates of the observations with and without the 1250 nm filter respectively.

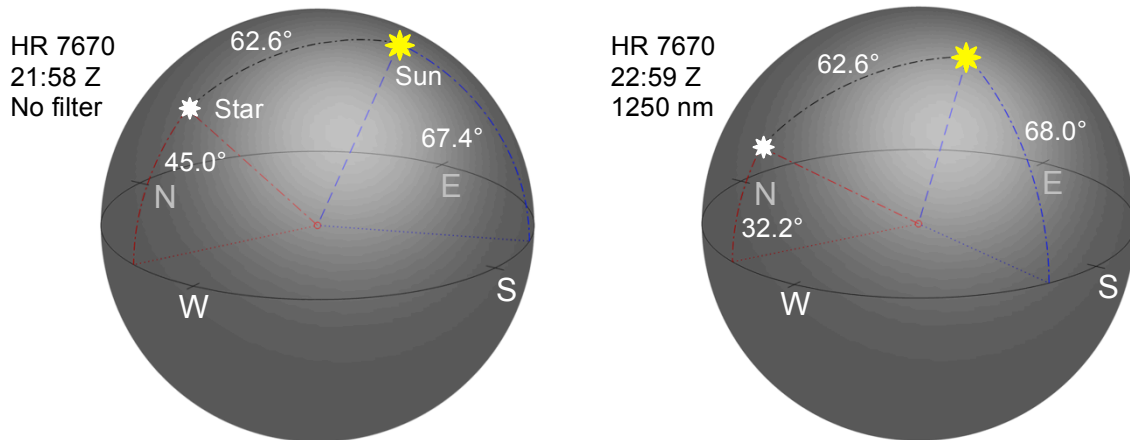


Figure 4. Observations of star HR 7670 (sequences 7 and 46) made with the AEOS telescope at 11:58 (left) and 12:59 (right) HST on 2014/3/19. The earlier observation was made with no filter ahead of the camera, while the later was made through the 1250 nm filter.

2.2 Photometric calibration from star images

To calibrate the photometry, the flux from the star must be isolated from the background by subtracting an estimate of the sky brightness distribution. In normal night-time observing in the near IR where the background flux is typically quite stable with time and position on sky, this is done by subtracting a near-simultaneous observation with identical exposure time on a nearby piece of blank sky. During the day, though, the sky brightness changes too rapidly and so we have adopted an alternative approach in which the background in the star data was modeled with modified Zernike polynomials. The basis functions, up to radial order 12, were defined and orthogonalized over a circular region containing most of the image but with the area around the star masked out. This approach, illustrated in Figure 5, was applied to data sets 7 and 46 representing respectively the case without and with the 1250 nm filter

in the beam. The circular regions masking out the star (and excluded from the background fit) were determined separately. After calculating the modal coefficients in the star data, the background estimate was synthesized and subtracted from the data including the area under the star, leaving only counts arising from the stellar flux. Since the stellar brightnesses in the near IR bands are known, it is then straightforward to calculate the conversion from pixel counts to magnitudes.

We note that the general pattern of brightness distribution of the sky background seen in Figure 5 was similar in all data sets examined. This was surprising, since the daytime sky is generally a very uniform illuminator. It seems likely then that the observed strong variations are attributable to the optics in the path ahead of the detector.

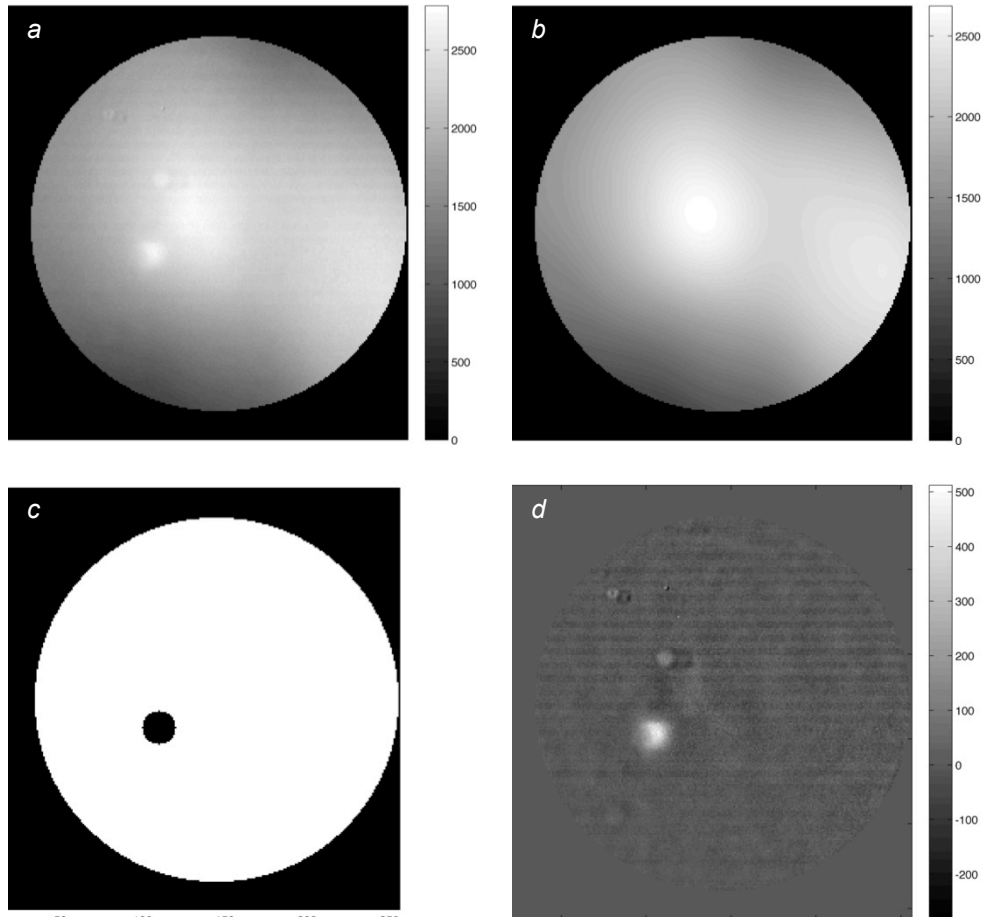


Figure 5. Example of the image data. a) Mean of 16 s of data recorded with no filter on HR 7670, after dark frame subtraction. b) Modeled sky background. c) Mask over which sky background is fitted. d) Difference between a and b showing the star.

2.3 Photometric uncertainty

Subtraction of incorrect background values from the star images would lead to potentially large errors in the photometric calibration. To estimate the uncertainty, the background subtraction procedure described above was applied to all the data sets with no star present, including masking out the region where the star would otherwise be. This should lead to a mean across the data sets of zero residual counts in that region, with a distribution of values that represents the uncertainty in the measured brightnesses of the stars. The result of the test was that the mean residual flux was indeed low at 0.06% of the flux of HR 7670, with a standard deviation of 0.2%. The formal uncertainty in the sky brightness results presented below is therefore just 2×10^{-3} magnitudes, although we hasten to note that this is likely far outweighed by uncertainties caused by unquantified systematic effects such as localized variations in atmospheric moisture and particulate density.

Some caution is required in the interpretation of the results presented in Section 3. The two data collection bands do not correspond directly to any of the standard broad photometric filters. In the case of the 1250 nm filter, the quoted results reflect the brightness that would be seen through a standard 2MASS J filter [9], and are in error to the extent that the mean brightness of HR 7670 per unit wavelength through our filter with 50 nm bandpass differs from the mean brightness per unit wavelength through the broader 2MASS filter with 162 nm bandpass. Given the known colors of the star, we estimate this error to be +0.01 magnitude. The photometry without the filter is calibrated against the calculated mean magnitude of the star over the full band of InGaAs sensitivity, which includes spectral regions of strong atmospheric extinction. The sky brightness results in this case represent the mean flux that would be seen through a set of filters of 15% bandwidth averaged over the range 0.9–1.6 μm . The variation within that range has not been quantified.

3 RESULTS

Details of the star observations used to establish the photometric calibration are shown in Table 1. Since the images all displayed similar strong variations of the signal across the FOV as seen in Figure 5, the sky brightness was determined in all cases only over the same small regions used to determine the stellar flux. In data sets with no star, the flux was summed directly from the images after dark subtraction. In data sets with a star, the sky flux was estimated from the fitted background. The analysis in Section 2.3 confirms that the difference between the two approaches is negligibly small.

Table 1. Details of the star observations used for photometric calibration.

Parameter	Data waveband	
	0.9–1.6 μm	1.20–1.25 μm
Single-frame exposure time	2 ms	16.65 ms
Star magnitude	4.50 mag	4.55 mag
Sky brightness per pixel	8.39 mag	8.36 mag
Pixel scale	0.25 arcsec	0.25 arcsec
Sky brightness	5.4 mag/arcsec²	5.3 mag/arcsec²

Although the data could not, of course, all be recorded simultaneously, we find that the time of day (within our limited 2.5 hour window) had a substantially smaller effect on the sky brightness than either the elevation angle or the solar phase angle. The photometric results as a function of elevation angle are shown in Figure 6, the two plots showing sky brightness with and without the filter. We have grouped the results into 10° bands of solar phase angle. The inserts in Figure 6 show the central angle of each band. Unsurprisingly, sky brightness increases at lower elevation angles and closer to the sun. The range in both bands is about 1.4 magnitudes, or a factor of about 3.6 in brightness. Note also that, for the measurements closest to the sun at 55° phase angle, the sky brightness plateaus at a lower elevation angle and at a brighter value for the data recorded with no filter than with the 1250 nm filter. That

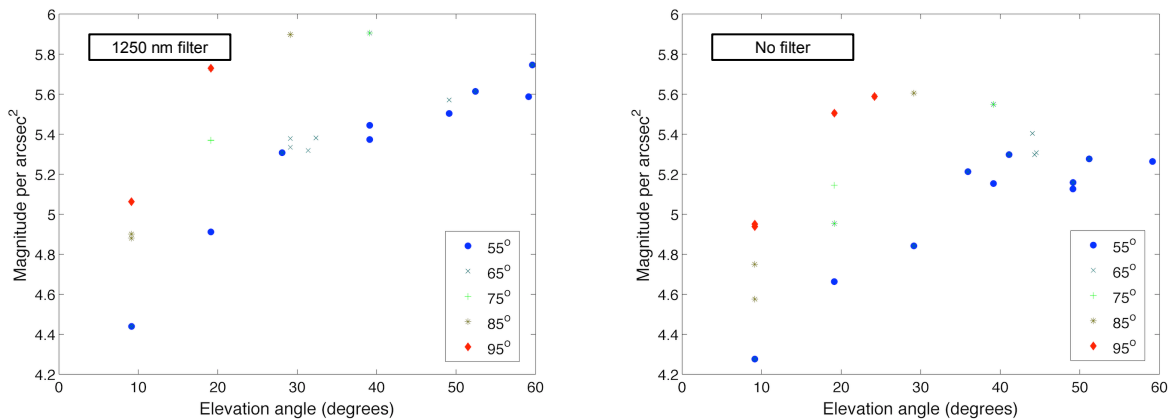


Figure 6. Sky brightness versus elevation angle with and without the 1250 nm filter. The results are grouped in ten degree increments of sun separation angle, shown by the different symbols.

is because the open case includes regions of the NIR spectrum where the atmosphere is optically thick, between the relatively clear I, J, and H windows. In those regions, sunlight scatters to larger characteristic angles than in the clear windows, analogous to a light bulb seen through frosted glass rather than clear glass.

Previous modeling by Jim, Gibson, & Pier [10, 11] used MODTRAN to calculate the expected sky brightness in the J and K bands along the GEO belt as seen from Haleakala, near the vernal equinox and the northern summer solstice. These days were chosen since they bracket the conditions in which the sun's diurnal track is closest to and furthest from the GEO belt. A detailed comparison to our results is difficult because the specific observing geometries are not well matched, although we note that our data were recorded on Day 78 of 2014, reasonably close to Day 83 modeled in [11]. Nevertheless, over the range of times of day (10:30 to 13:00 local time), elevation angle (9° to 60°), and solar phase angle (50° to 100°) spanned by our data, the J-band plots for Day 83 in Figures 6 and 7 of reference [11] show a range from approximately 4.0 to 6.2 mag/arcsec², which is close to the range of 4.4 to 6.2 mag/arcsec² found in our results.

4 A NEAR-IR WFS FOR DORA

Encouraged by this result, we are proceeding to build a near-IR WFS for the AEOS telescope, with delivery expected in October 2014. The background photon noise from the sky will be better than in the V band [5], where sky brightness is typically in the range 2.5–4.5 mag per arcsec², and will not prevent wave-front information from being collected on bright satellites. The WFS is of the Shack-Hartmann type with interchangeable lenslet arrays to adjust the spatial sampling of the wave front in response to specific SNR regimes. The layout is illustrated in the solid model of Figure 7. A fast steering mirror (FSM) at an image of the telescope pupil serves to reduce overall image motion and maintain the mean position of the Shack-Hartmann images centered. The FSM is driven on the basis of the mean spot motion observed on the WFS.

The detector itself is a SU640HSX-1.7RT InGaAs camera from Sensors Unlimited, running a 128×128 region of interest at 500 frames per second. The camera is not cryogenically cooled and does not exhibit the lowest read noise that it otherwise might, but the frame rate is low enough to ensure that the noise is below the limiting threshold set by the background shot noise. While not fast for a conventional WFS operating in an adaptive optics system, the speed is more than adequate since there is no latency between the wave-front information and the speckle images: the processing happens after detection in the computer. There is also no numerical integrator in the loop to impose further phase delay as there is with an AO system.

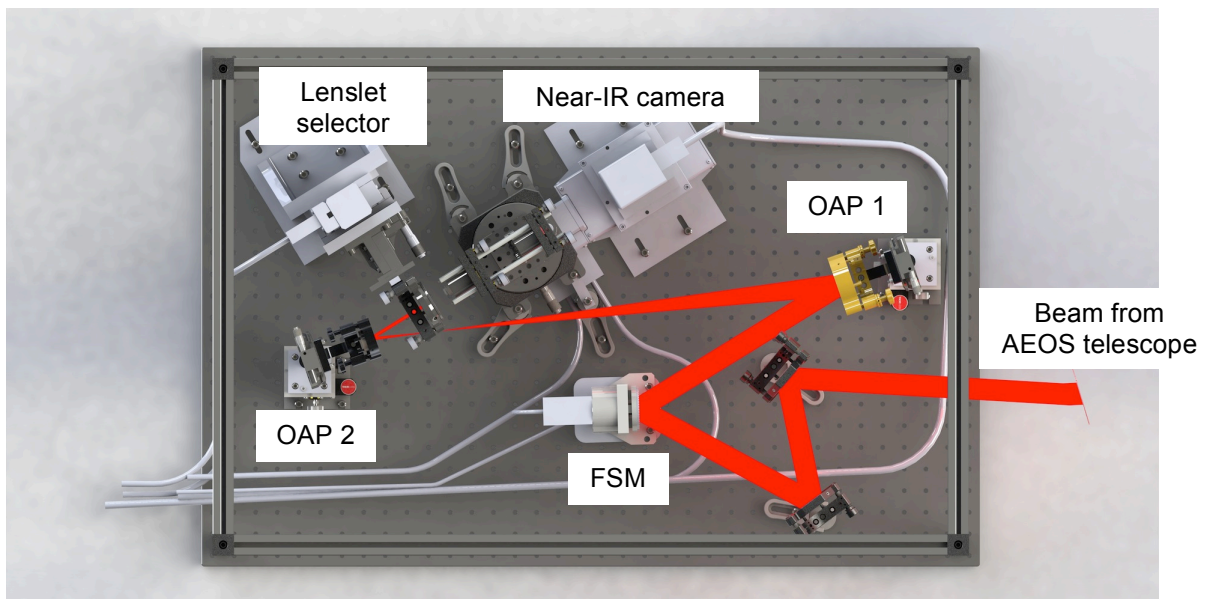


Figure 7. Layout of the WFS for the Advanced Research Daylight Imaging experiment at the AEOS 3.6 m telescope. The WFS is constructed on a 2×3 foot optical breadboard.

The WFS detector is sensitive to the same range of wavelengths as the SC6000 used in our study, and our results suggest that the sky brightness does not change substantially over that range. We will therefore use no filter in front of the WFS, accepting the widest band possible, in order to maximize the SNR on tracked satellites.

5 CONCLUDING REMARKS

This single snapshot of near-IR sky brightness above Haleakala is of practical use: it has allowed us to move ahead with a WFS for daylight satellite imaging at AEOS in a way that exploits a greater optical bandwidth than previous instruments have used. But it is by no means the last word on the subject. The data collection was brief, on a single day, and although the sky was clear during the observations, no specific controls or monitoring of weather were implemented. Such uncontrolled effects are likely the cause of the significant scatter in our results. Since the SWIR bands are likely to be of great importance to SSA, we look forward to more extensive campaigns conducted from key SSA sites like Haleakala and the Starfire Optical Range. With the implementation of an appropriate camera and data recording system, a long-term campaign covering all time scales and regions of the sky could readily be automated as an adjunct to normal operations with other sensors.

6 ACKNOWLEDGEMENTS

This work has been supported by the United States Air Force Research Laboratory, Directed Energy Directorate, under contract FA9451-12-C-0004. The opinions, findings and conclusions expressed in this paper are those of the authors and do not necessarily reflect the views of the United States Air Force. We are most grateful to the Boeing team at the MSSS for their assistance in acquiring the data analyzed in this study.

7 REFERENCES

- [1] Calef, B. "Improving imaging through turbulence via aperture partitioning," in *Visual Information Processing XIX* (Proc. SPIE), eds. Z-U. Rahman, S. E. Reichenbach, & M. A. Neifeld, 7701, 77010G (2010)
- [2] Hart, M. et al., "Multi-frame blind deconvolution for imaging in daylight and strong turbulence conditions," in *Unconventional Imaging, Wavefront Sensing, and Adaptive Coded Aperture Imaging and Non-Imaging Sensor Systems* (Proc. SPIE), eds. J. J. Dolne, S. Rogers, D. Casasent, T. J. Karr, & V. L. Gamiz, 8165, 81650L (2011)
- [3] Hope, D., Hart, M., Jefferies, S., and Nagy, J. "Imaging satellites at high noon," these proceedings
- [4] LaBonte, B. "Sky brightness measurements at Haleakala, 1955–2002," *Solar Physics*, 217, 367-381 (2003)
- [5] Lin, H. & Penn, M. J. "The Advanced Technology Solar Telescope site survey sky brightness monitor," *Pub. Ast. Soc. Pac.* 116, 652–666 (2004)
- [6] <http://www.edmundoptics.com/optics/optical-filters/bandpass-filters/hard-coated-od4-50nm-bandpass-filters/85909>
- [7] The BPGS catalog is available at <ftp://ftp.stsci.edu/cdbs/grid/bpgs/>
- [8] <http://simbad.u-strasbg.fr/simbad/sim-id?Ident=HD+190360>
- [9] Cohen, M., Wheaton, W. A., and Megeath, S. T. "Spectral irradiance calibration in the infrared. XIV. The absolute calibration of 2MASS," *Astron. J.*, 126, 1090–1096 (2003)
- [10] Jim, K. T. C., Gibson, B. N., and Pier, E. A. "Daytime sky brightness modeling of Haleakala," AMOS Technical Conference (2011)
- [11] Jim, K. T. C., Gibson, B. N., and Pier, E. A. "Daytime sky brightness modeling of Haleakala along the GEO belt," AMOS Technical Conference (2012)

APPENDIX

Table A1. Full list of observations and estimated sky brightness.

#	Observation time (UTC)	Object	Integration time (μ s)	AZ ($^{\circ}$)	EL ($^{\circ}$)	Sun AZ ($^{\circ}$)	Sun EL ($^{\circ}$)	Solar angle	Filter	Magnitude per arcsec ²
1	20:33	HD166780	16650	327.2	34.7	122.1	53.9	88.8	Y	6.23
2	20:40	58 Aql	16650	241.2	52.4	124.0	55.3	60.5	Y	5.61
3	20:43	HR 8020	16650	335.8	59.6	124.9	55.9	61.9	Y	5.75
4	21:51	HR 8020	3983	321.9	51.2	153.0	66.6	61.9	N	5.28
5	21:53	HD 166780	3983	325.5	24.2	154.1	66.8	88.8	N	5.59
6	21:56	58 Aql	3983	254.5	35.9	155.9	67.1	60.5	N	5.21
7	21:58	HR 7670	3983	292.1	44.5	157.1	67.3	63.1	N	5.31
8	21:59	HR 7670	1983	292.1	44.3	157.7	67.3	63.2	N	5.30
9	22:00	11 Sge	1983	274.6	41.1	158.3	67.4	61.4	N	5.30
10	22:04	HR 7699	3983	298.4	44.0	160.8	67.8	63.7	N	5.40
11	22:15	Sky	3983	0.0	9.1	167.9	68.5	101.9	N	4.95
12	22:17	Sky	3983	0.0	9.1	169.3	68.6	101.9	N	4.94
13	22:18	Sky	3983	0.0	19.1	169.9	68.6	92.0	N	5.50
14	22:19	Sky	3983	0.0	29.1	170.6	68.6	82.0	N	5.61
15	22:20	Sky	3983	0.0	39.1	171.3	68.7	72.0	N	5.55
16	22:20	Sky	3983	0.0	49.1	171.3	68.7	62.0	N	5.16
17	22:21	Sky	3983	0.0	59.1	172.0	68.7	52.0	N	5.26
18	22:23	Sky	1983	90.0	9.1	173.3	68.8	79.1	N	4.58
19	22:24	Sky	1983	90.0	19.1	174.0	68.8	70.0	N	4.95
20	22:24	Sky	1983	90.0	29.1	174.0	68.8	60.9	N	4.84
21	22:25	Sky	1983	90.0	39.1	174.7	68.8	52.1	N	5.15
22	22:26	Sky	1983	180.0	9.1	175.4	68.8	59.7	N	4.28
23	22:27	Sky	1983	180.0	19.1	176.1	68.9	49.8	N	4.66
24	22:28	Sky	1983	280.0	9.1	176.8	68.9	86.2	N	4.75
25	22:29	Sky	1983	280.0	19.1	177.5	68.9	76.6	N	5.14
26	22:30	Sky	1983	280.0	49.1	178.2	68.9	48.9	N	5.13
27	22:37	Sky	1983	280.0	9.1	183.0	68.9	84.0	Y	4.88
28	22:38	Sky	3983	280.0	9.1	183.7	68.9	83.7	Y	4.88
29	22:38	Sky	3983	280.0	19.1	183.7	68.9	74.4	Y	5.37
30	22:39	Sky	3983	280.0	29.1	184.4	68.8	65.0	Y	5.38
31	22:40	Sky	3983	280.0	39.1	185.1	68.8	55.6	Y	5.44
32	22:42	Sky	3983	179.1	9.1	186.5	68.8	59.9	Y	4.44
33	22:43	Sky	3983	179.1	19.1	187.2	68.8	49.9	Y	4.91
34	22:43	Sky	3983	89.1	9.1	187.2	68.8	84.4	Y	4.90
35	22:44	Sky	3983	89.1	19.1	187.8	68.7	75.3	Y	5.37
36	22:44	Sky	3983	89.1	29.1	187.8	68.7	66.1	Y	5.33
37	22:45	Sky	3983	89.1	39.1	188.5	68.7	57.2	Y	5.37
38	22:46	Sky	3983	89.1	49.1	189.2	68.7	48.5	Y	5.50
39	22:47	Sky	3983	359.1	9.1	189.9	68.6	101.9	Y	5.06
40	22:47	Sky	3983	359.1	19.1	189.9	68.6	91.9	Y	5.73
41	22:48	Sky	3983	359.1	29.1	190.6	68.6	81.9	Y	5.90
42	22:48	Sky	3983	359.1	39.1	190.6	68.6	71.9	Y	5.91
43	22:49	Sky	3983	359.1	49.1	191.2	68.5	62.0	Y	5.57
44	22:49	Sky	3983	359.1	59.1	191.2	68.5	52.1	Y	5.59
45	22:56	11 Sge	16650	278.6	28.1	195.9	68.1	61.4	Y	5.31
46	22:59	HR 7670	16650	293.2	31.4	197.8	67.9	63.1	Y	5.32
47	23:00	HR 7699	16650	298.5	32.4	198.4	67.9	63.9	Y	5.38

Column heading	Description
#	Sequence number of the observation
Observation time (UTC)	Time of the start of the observation
Object	Object name (either sky or star designator).
Integration time (μ s)	Integration time of each frame of an observing sequence
AZ, EL	Azimuth and elevation angles of the observation (at the start of the sequence for the stars)
Sun AZ, Sun EL	Azimuth and elevation angles of the sun during the observation
Solar angle	Angular distance between the observation point and the sun
Filter	Indicates the use or not of the 1250 nm filter
Magnitude	Estimated sky brightness expressed as magnitudes per arcsec ² for a filter of 18% bandwidth